



Article

Micro-Doppler Parameters Extraction of Precession Cone-Shaped Targets Based on Rotating Antenna

Zhihao Wang ¹, Ying Luo ^{1,2,*}, Kaiming Li ¹, Hang Yuan ¹ and Qun Zhang ^{1,2}

¹ Information and Navigation College, Air Force Engineering University, Xi'an 710077, China; afeuwzh@163.com (Z.W.); likaiming1982@163.com (K.L.); yuanhang517300@163.com (H.Y.); afeuzq@163.com (Q.Z.)

² Key Laboratory of Wave Scattering and Remote Sensing Information, Fudan University, Shanghai 200433, China

* Correspondence: luoying2002521@163.com

Abstract: Micro-Doppler is regarded as a unique signature of a target with micro-motions. The sophisticated recognition of the cone-shaped targets can be realized through the micro-Doppler effect. However, it is difficult to extract the micro-motion features perpendicular to the radar line of sight (LOS) effectively. In this paper, a micro-Doppler parameters extraction method of the cone-shaped targets is put forward based on the rotating antenna. First, a new radar configuration is proposed, in which an antenna rotates uniformly on a fixed circle, thus producing Doppler frequency shift. Second, the expression of the micro-Doppler frequency shift induced by the precession cone-shaped target is derived. Then, the micro-Doppler curves of point scatterers at the cone top and bottom are separated by the smoothness of the curves, and the empirical mode decomposition (EMD) method is utilized for the detection and estimation of the coning frequency. Finally, the micro-motion components perpendicular to the radar LOS are inverted by the peak of micro-Doppler frequency curve. Simulation results prove the effectiveness and robustness of the proposed method.

Keywords: rotating antenna; micro-Doppler; precession cone-shaped target; parameters extraction; EMD



Citation: Wang, Z.; Luo, Y.; Li, K.; Yuan, H.; Zhang, Q. Micro-Doppler Parameters Extraction of Precession Cone-Shaped Targets Based on Rotating Antenna. *Remote Sens.* **2022**, *14*, 2549. <https://doi.org/10.3390/rs14112549>

Academic Editors: Junjie Wu, Xiaolong Chen, Jibin Zheng and Bo Chen

Received: 10 April 2022

Accepted: 24 May 2022

Published: 26 May 2022

Publisher's Note: MDPI stays neutral with regard to jurisdictional claims in published maps and institutional affiliations.



Copyright: © 2022 by the authors. Licensee MDPI, Basel, Switzerland. This article is an open access article distributed under the terms and conditions of the Creative Commons Attribution (CC BY) license (<https://creativecommons.org/licenses/by/4.0/>).

1. Introduction

The micro-Doppler effect is a physical phenomenon caused by the micro-motion of objects and their components, and it is regarded as a unique characteristic of objects [1–3]. The micro-Doppler effect can provide additional information for target classification and recognition [4–7]. A large number of ballistic missiles are cone-shaped targets. In the midcourse or terminal of the flight, the motion state usually presents the compound motion of spinning and coning, namely precession. Therefore, the parameters estimation of precession cone-shaped targets has attracted much attention [8–11].

Monostatic radar is applied to parameters estimation of precession cone-shaped targets [12–14]. In [13], by estimating and analyzing the micro-range of the target scattering center, high-resolution three-dimensional (3D) imaging of the target, together with the precession angle and radar LOS can be accurately obtained. The literature [14] proposed a cycle shift smoothed L0 algorithm based on compressive sensing, which can achieve high-resolution imaging of precession cone-shaped targets by exploiting sparse aperture. The monostatic radar can extract the radial micro-motion features. However, when the targets have no micro-motion component in the radar LOS, the micro-motion features cannot be extracted effectively.

Bistatic/multistatic radar can detect targets from different angles, and the micro-motion features of the targets can be reconstructed by using correlation processing [15–19], to solve the problem that monostatic radar cannot detect the micro-motion component

perpendicular to the radial direction. In [16], a single-range interferometric imaging algorithm is proposed, in which the target echoes can be obtained through three antennas placed in the shape of “L”, and the interferometric phases of scatterers can be obtained after time-frequency analysis, to obtain the two-dimensional image of the target. The literature [17,18] proposed a new ballistic target discrimination (BTD) framework based on distributed radar network. 1D normalized echo was used for signal decomposition to save computing resources. This method achieved effective parameter estimation for real-time BTD. Literature [19] has established a classification model and a robust framework combining different micro-Doppler-based classification techniques to effectively distinguish ballistic targets from false targets. However, it is extremely difficult to remove the phase coupling. In addition, the high cost of multiple-antenna configuration limits the practical application.

In recent years, orbital angular momentum (OAM) has attracted increasing attention due to its unique properties [20–22]. In addition to traditional linear momentum, it can also generate rotation angular momentum, thus offering new degrees of freedom. The helical phase front structure of OAM can be used to extract the micro-motion features perpendicular to the radial direction [23–26]. In [23], geometric and micro-motion parameters of precession cone-shaped target were obtained by the combination of the linear Doppler and angular Doppler when the micro-motion plane is perpendicular to the radar LOS. In [26], it theoretically deduced the angular Doppler frequency shift of the target under the conditions of rotating plane deflection and off-axis and inverted the target’s motion information according to the maximum value of the echo time-frequency curves. However, the angular Doppler frequency shift is closely related to the detection range and OAM mode number. Under the conditions of long-range, the angular Doppler shift is very small, so the micro-motion features of targets cannot be obtained effectively. In addition, the vortex electromagnetic wave (EM) waves used in radar imaging and recognition are generated by the uniform circular array (UCA) [27,28]. The more array elements are, the more mode number can be generated. Therefore, the size of the array limits the OAM mode number. In general, there are still many problems to be solved in extracting the micro-motion features using vortex EM radar.

To solve the above problems, this paper puts forward a method to extract the micro-Doppler features of precession cone-shaped target perpendicular to the radar LOS based on the rotating antenna. First, a new radar configuration is proposed, in which an antenna rotates uniformly on a fixed circle, thus producing Doppler frequency shift. Second, the expression of micro-Doppler frequency shift induced by the precession cone-shaped target is derived, and the skeleton is extracted from the echo micro-Doppler frequency curve obtained by short-time Fourier transform (STFT). Then, the micro-Doppler curves of point scatterers at the cone top and bottom are separated by the smoothness of the curves, and the EMD method is utilized for the detection and estimation of the coning frequency. Finally, by the combination of the extracted micro-Doppler information and high-resolution one-dimensional (1D) range information, the geometric and micro-motion parameters of the precession cone-shaped target are effectively estimated when the micro-motion plane is perpendicular to the radar LOS. This paper provides a new idea for the micro-Doppler features extraction and recognition in the specific scene.

The rest of this paper is organized as follows. Section 2 presents a new radar configuration based on the rotating antenna. The radar signal processing method is introduced and the micro-Doppler expression of the rotating target whose micro-motion plane is perpendicular to the radar LOS is derived in this section. The micro-Doppler parameters’ estimation method of the precession cone-shaped target is elaborated in Section 3, in which the geometric and micro-motion parameters can be obtained by the combination of high-resolution 1D range and micro-Doppler information. In Section 4, the effectiveness and robustness of the proposed method are discussed through simulations. Finally, conclusions are described in Section 5.

2. Micro-Doppler Characteristic Analysis of Precession Cone-Shaped Target

The radar position is shown in Figure 1, $OXYZ$ is the radar Cartesian coordinate system. An antenna rotates at frequency f_a and radius a on the XOY plane taking the origin point O as the center of the circle. The antenna Q is located at $(a, 0, 0)^T$ when the time is zero and moves in a counterclockwise direction, where the superscript 'T' means transposition. θ_r and φ_r are the polar angle and azimuth angle of the radar LOS respectively, and $\theta_r \in [0, \pi], \varphi_r \in [0, 2\pi]$. Therefore, the unit vector of the radar LOS can be expressed as $\mathbf{n}_{LOS} = (n_x, n_y, n_z)^T = (\sin \theta_r \cos \varphi_r, \sin \theta_r \sin \varphi_r, \cos \theta_r)^T$. Both transmitting and receiving signals are carried out in Q . A wideband radar is placed at O to obtain the high-resolution 1D range of the target.

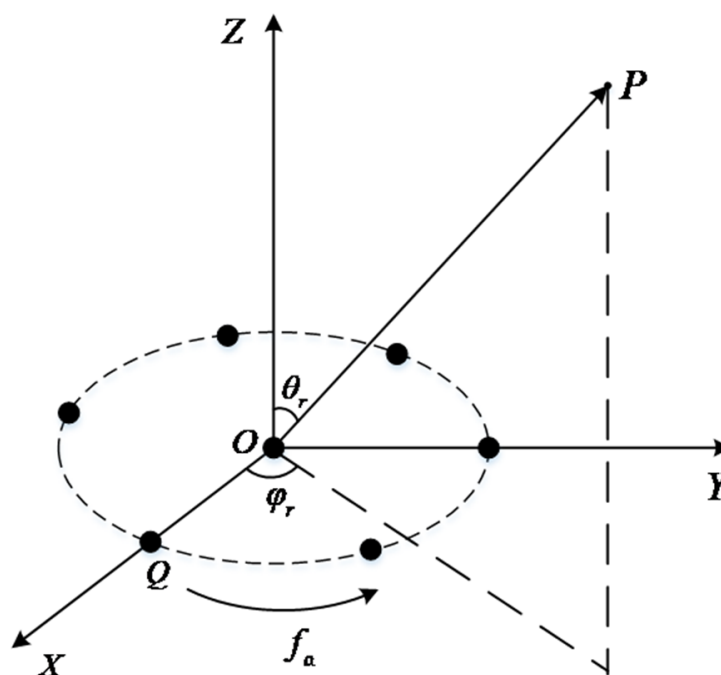


Figure 1. Diagram of radar configuration.

Suppose that there exists a cone-shaped target in space. In addition to spinning around its axis of symmetry to keep stationary while going on a translation along the radar LOS, the cone-shaped target will undergo a coning motion about the radar LOS with the angular velocity $2\pi f_c \mathbf{n}_{LOS}$. The spinning and the coning make up precession, and the precession angle is θ_c . The geometry relationship of the precession cone-shaped target is shown in Figure 2. The height of the cone-shaped target is H , the radius of the cone bottom is r_c , and the height from the center of mass O' to the cone bottom is h . The spherical coordinate of O' is $(R_0, \theta_r, \varphi_r)$, where R_0 denotes the radial distance from O' to O . Assume that the target is a smooth cone. Therefore, the influence of spinning motion on radar echoes can be ignored according to its rotation symmetry. At this point, the precession of the cone-shaped target can be regarded as a scatterer rotating around the radar LOS with the angular velocity $2\pi f_c \mathbf{n}_{LOS}$ and radius r .

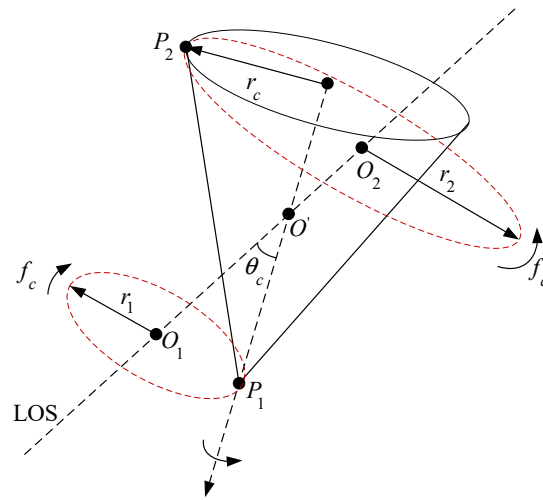


Figure 2. The geometric relationship of the precession cone-shaped target.

When the cone-shaped target translates along with the radar LOS, the monostatic radar cannot effectively extract the micro-Doppler perpendicular to the radial direction. The circular motion of the antenna will cause the change of the radial distance, which will induce Doppler frequency shift, from which the geometric and micro-motion parameters of the cone-shaped target can be inversely calculated.

The Cartesian coordinate of Q at slow-time t_m is

$$OQ = (a \cdot \cos(2\pi f_a t_m), a \cdot \sin(2\pi f_a t_m), 0)^T \tag{1}$$

It is assumed that a point scatterer P rotates around the point O_p with radius r and angular velocity $2\pi f_c \mathbf{n}_{LOS} = 2\pi f_c (n_x, n_y, n_z)^T$, the scatterer point P can be represented in the target-local coordinate system by

$$O_p P = (r \cdot \cos(2\pi f_c t_m), r \cdot \sin(2\pi f_c t_m), 0)^T \tag{2}$$

The position vector of P in the radar Cartesian coordinate system $OXYZ$ can be written as

$$OP = OO_p + R_{init} \times O_p P \tag{3}$$

where OO_p is the position vector of O_p in $OXYZ$.

$$OO_p = R_0 \times \mathbf{n}_{LOS} = (R_0 \sin \theta_r \cos \varphi_r, R_0 \sin \theta_r \sin \varphi_r, R_0 \cos \theta_r)^T \tag{4}$$

R_{init} is the Euler rotation matrix [29], which is decided by the initial Euler angles $(\varphi_r - \frac{\pi}{2}, \theta_r, 0)$, and can be defined by

$$R_{init} = \begin{bmatrix} 1 & 0 & 0 \\ 0 & 1 & 0 \\ 0 & 0 & 1 \end{bmatrix} \begin{bmatrix} 1 & 0 & 0 \\ 0 & \cos \theta_r & \sin \theta_r \\ 0 & -\sin \theta_r & \cos \theta_r \end{bmatrix} \begin{bmatrix} \sin \varphi_r & -\cos \varphi_r & 0 \\ \cos \varphi_r & \sin \varphi_r & 0 \\ 0 & 0 & 1 \end{bmatrix} \tag{5}$$

$$= \begin{bmatrix} \sin \varphi_r & \cos \varphi_r \cos \theta_r & \cos \varphi_r \sin \theta_r \\ -\cos \varphi_r & \sin \varphi_r \cos \theta_r & \sin \varphi_r \sin \theta_r \\ 0 & -\sin \theta_r & \cos \theta_r \end{bmatrix}$$

Therefore, OP can be written as

$$\begin{aligned}
 \mathbf{OP} &= \begin{pmatrix} R_0 \sin \theta_r \cos \varphi_r \\ R_0 \sin \theta_r \sin \varphi_r \\ R_0 \cos \theta_r \end{pmatrix} + \begin{bmatrix} \sin \varphi_r & \cos \varphi_r \cos \theta_r & \cos \varphi_r \sin \theta_r \\ -\cos \varphi_r & \sin \varphi_r \cos \theta_r & \sin \varphi_r \sin \theta_r \\ 0 & -\sin \theta_r & \cos \theta_r \end{bmatrix} \times \begin{pmatrix} r \cdot \cos(2\pi f_c t_m) \\ r \cdot \sin(2\pi f_c t_m) \\ 0 \end{pmatrix} \\
 &= \begin{pmatrix} r \cdot \sin \varphi_r \cos(2\pi f_c t_m) + r \cdot \cos \varphi_r \cos \theta_r \sin(2\pi f_c t_m) + R_0 \sin \theta_r \cos \varphi_r \\ -r \cdot \cos \varphi_r \cos(2\pi f_c t_m) + r \cdot \sin \varphi_r \cos \theta_r \sin(2\pi f_c t_m) + R_0 \sin \theta_r \sin \varphi_r \\ -r \cdot \sin \theta_r \sin(2\pi f_c t_m) + R_0 \cos \theta_r \end{pmatrix}
 \end{aligned} \tag{6}$$

Thus, the range vector \mathbf{QP} from the radar Q to the scatterer at P can be derived as

$$\begin{aligned}
 \mathbf{QP} &= \mathbf{OP} - \mathbf{OQ} \\
 &= \begin{pmatrix} r \cdot \sin \varphi_r \cos(2\pi f_c t_m) + r \cdot \cos \varphi_r \cos \theta_r \sin(2\pi f_c t_m) + R_0 \sin \theta_r \cos \varphi_r - a \cos(2\pi f_a t_m) \\ -r \cdot \cos \varphi_r \cos(2\pi f_c t_m) + r \cdot \sin \varphi_r \cos \theta_r \sin(2\pi f_c t_m) + R_0 \sin \theta_r \sin \varphi_r - a \sin(2\pi f_a t_m) \\ -r \cdot \sin \theta_r \sin(2\pi f_c t_m) + R_0 \cos \theta_r \end{pmatrix}
 \end{aligned} \tag{7}$$

And the scalar range becomes

$$r_p(t_m) = \sqrt{a^2 + r^2 + R_0^2 - 2aR_0 \sin \theta_r \cos(2\pi f_a t_m - \varphi_r) + 2ar(\cos(2\pi f_c t_m) \sin(2\pi f_a t_m - \varphi_r) - \cos \theta_r \sin(2\pi f_c t_m) \cos(2\pi f_a t_m - \varphi_r))} \tag{8}$$

Compared with R_0 , the rotation radius a and the cone bottom radius r have negligible effects on the instantaneous radial distance $r_p(t_m)$. Therefore, the Fresnel approximation can be applied to (8). $r_p(t_m)$ can be expressed in the spherical coordinate system as

$$r_p(t_m) \approx R_0 + \frac{a^2 + r^2}{2R_0} - a \sin \theta_r \cos(2\pi f_a t_m - \varphi_r) + \frac{ar(\cos(2\pi f_c t_m) \sin(2\pi f_a t_m - \varphi_r) - \cos \theta_r \sin(2\pi f_c t_m) \cos(2\pi f_a t_m - \varphi_r))}{R_0} \tag{9}$$

If the rotating antenna transmits a single frequency continuous-wave signal

$$S(t) = \exp(j2\pi f_0 t) \tag{10}$$

where t is the fast-time, f_0 is the carrier frequency, j is the imaginary unit.

Within the duration of a pulse, the scatterer and radar can be approximately regarded as relatively static, satisfying the assumption of “stop-go” model, then the received echo signal can be written as

$$S_{echo}(t_m, t) = \exp(j2\pi f_0(t - \tau_p(t_m))) \tag{11}$$

where $\tau_p(t_m) = \frac{2r_p(t_m)}{c}$, c denotes the wave propagation velocity.

After conducting baseband transform on $s_{echo}(t_m, t)$, it can be obtained that

$$\begin{aligned}
 S_c(t_m) &= \exp\left(j\frac{4\pi}{\lambda}r_p(t_m)\right) = \exp\left(-j\frac{4\pi}{\lambda}\left(R_0 + \frac{a^2+r^2}{2R_0}\right)\right) \exp\left(j\frac{4\pi}{\lambda}a \cdot \sin \theta_r \cos(2\pi f_a t_m - \varphi_r)\right) \\
 &\times \exp\left(-j\frac{4\pi}{\lambda}\frac{ar}{R_0}(\cos(2\pi f_c t_m) \sin(2\pi f_a t_m - \varphi_r) - \cos \theta_r \sin(2\pi f_c t_m) \cos(2\pi f_a t_m - \varphi_r))\right)
 \end{aligned} \tag{12}$$

To eliminate the micro-Doppler effect merely induced by antenna rotating, a phase compensation function $S_{com}(t_m)$ is introduced into the echoes.

$$S_{com}(t_m) = \exp\left(-j\frac{4\pi}{\lambda}a \cdot \sin \theta_r \cos(2\pi f_a t_m - \varphi_r)\right) \tag{13}$$

Multiplying $S_{com}(t_m)$ with $S_c(t_m)$, it can be obtained that

$$\begin{aligned}
 S(t_m) &= S_c(t_m) \times S_{com}(t_m) = \exp\left(-j\frac{4\pi}{\lambda}\left(R_0 + \frac{a^2+r^2}{2R_0}\right)\right) \times \\
 &\exp\left(j\frac{4\pi}{\lambda}\frac{ar}{R_0}(\cos(2\pi f_c t_m) \sin(2\pi f_a t_m - \varphi_r) - \cos \theta_r \sin(2\pi f_c t_m) \cos(2\pi f_a t_m - \varphi_r))\right)
 \end{aligned} \tag{14}$$

The change process of phase with slow-time can be derived as

$$\Phi(t_m) = -\frac{4\pi}{\lambda}\left(R_0 + \frac{a^2+r^2}{2R_0}\right) + \frac{4\pi}{\lambda}\frac{ar}{R_0}(\cos(2\pi f_c t_m) \sin(2\pi f_a t_m - \varphi_r) - \cos \theta_r \sin(2\pi f_c t_m) \cos(2\pi f_a t_m - \varphi_r)) \tag{15}$$

By taking the slow-time derivative of the phase, the micro-Doppler frequency shift induced by the rotation of scatterer perpendicular to the radar LOS can be derived as

$$\begin{aligned} f_d(t_m) &= \frac{1}{2\pi} \frac{d\Phi(t_m)}{dt_m} \\ &= \frac{2\pi}{\lambda} \frac{ar}{R_0} ((f_a - f_c)(1 + \cos \theta_r) \cos(2\pi(f_a - f_c)t_m - \varphi_r) + (f_a + f_c)(1 - \cos \theta_r) \cos(2\pi(f_a + f_c)t_m - \varphi_r)) \end{aligned} \quad (16)$$

from which it can be found that through this radar configuration, the expression of micro-Doppler frequency induced by the rotation of scatterer perpendicular to the radar LOS does not appear as a sinusoidal curve anymore but as a composition of two sinusoidal components. The frequencies of the two sinusoidal components are $f_a - f_c$ and $f_a + f_c$ respectively. Therefore, the period is the lowest common multiple of the periods of the two components, which can be written as

$$T_{fd} = \frac{k_1}{|f_a - f_c|} = \frac{k_2}{f_a + f_c}, k_1, k_2 \in N \quad (17)$$

where T_{fd} is the period of the micro-Doppler frequency curve and N is the set of natural numbers.

To verify the correctness of the above derivation processes, it is assumed that the rotating antenna operates at 75 GHz. A scatterer, which is located at ($R_0 = 2$ Km, $\theta_r = \pi/30$ rad, $\varphi_r = \pi/3$ rad), is rotating about the radar LOS with an initial Euler angle, rotation frequency $f_c = 8$ Hz and rotation radius $r = 1$ m. The antenna rotates around O on the XYZ plane with a radius $a = 5$ m and a frequency $f_a = 4$ Hz. The radar pulse repetition frequency (PRF) is 1000 Hz. The irradiation time is 3 s. After STFT, the echo micro-Doppler frequency curve is shown in Figure 3a. The true and approximate values of the theoretical micro-Doppler frequency shift can be obtained by the derivative of the true and approximate phases with respect to slow-time respectively, and the results are shown in Figure 3b, which shows that the true value is in good agreement with approximate value. The maximum value of the echo micro-Doppler frequency curve is 33.33 Hz and the period is 0.252 s. According to (17), the theoretical period of the micro-Doppler frequency curve is the lowest common multiple of $\frac{1}{4}$ s and $\frac{1}{12}$ s (i.e., 0.25 s), and the theoretical maximum value of micro-Doppler frequency is 34.47 Hz. Therefore, echo micro-Doppler frequency curve is identical to the theoretical frequency of the micro-Doppler frequency curve, which proves the correctness of the above derivation processes.

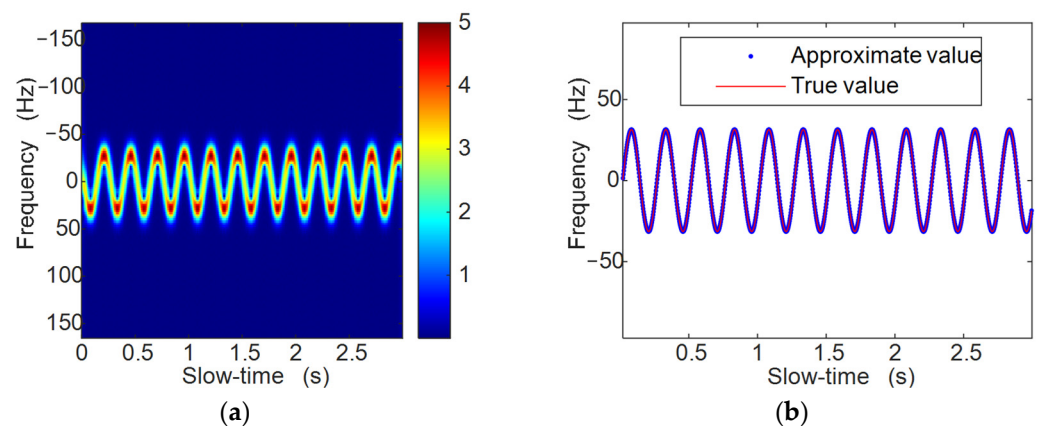


Figure 3. Simulations of the micro-Doppler effect of a scatterer with rotation. (a) The echo micro-Doppler frequency curve. (b) Theoretical micro-Doppler frequency curve.

3. Parameters Estimation of Precession Cone-Shaped Target

It is assumed that there are two strong scatterer points of the cone-shaped target, one of which is on the top of the cone and located at P_1 , and the other is on the bottom of the cone and located at P_2 . P_1 and P_2 undergo a coning motion about the radar LOS with centers O_1 and O_2 respectively. The spherical coordinates of O_1 and O_2 can be written as

$(R_1, \theta_r, \varphi_r)$ and $(R_2, \theta_r, \varphi_r)$. The rotation radius of P_1 and P_2 can be obtained according to the geometric relationship of the cone.

$$\begin{cases} R_1 = R_0 - (H - h) \cos \theta_c \\ R_2 = R_0 + h \cos \theta_c - r_c \sin \theta_c \end{cases} \tag{18}$$

$$\begin{cases} r_1 = (H - h) \sin \theta_c \\ r_2 = h \sin \theta_c + r_c \cos \theta_c \end{cases} \tag{19}$$

It can be concluded that the initial phase of the scatterer at the cone bottom is π larger than that at the cone top. The parameters of the precession cone-shaped target can be obtained by jointly analyzing the micro-Doppler frequencies of the scatterers at the cone top and bottom. According to (16), the slow-time-varying micro-Doppler frequencies of precession cone-shaped target can be derived as

$$\begin{aligned} f_{d-pci}(t_m) &= \frac{2\pi a r_i}{\lambda R_i} ((f_a - f_c)(1 + \cos \theta_r) \cos(2\pi(f_a - f_c)t_m - \varphi_i) + (f_a + f_c)(1 - \cos \theta_r) \cos(2\pi(f_a + f_c)t_m - \varphi_i)) \\ &= \frac{2\pi a r_i}{\lambda R_i} A(t_m), \quad i = 1, 2 \end{aligned} \tag{20}$$

Before EMD decomposition, it is necessary to separate the micro-Doppler curves of point scatterers at the cone top and bottom. According to Equation (20), the derivatives of the micro-Doppler with respect to slow-time are continuous and smooth. Based on this fact, the separation of micro-Doppler curves can be achieved. Assume the skeleton image is a $M_s \times N_s$ matrix, one m-D curve consists of N' points. The index of the n' point on the curve in the matrix is $(x_{n'}, y_{n'})$. Then the optimization model can be expressed as [15]

$$\begin{aligned} \min f(x_{n'}, y_{n'}) &= \left| \frac{x_{n'} - x_{n'-1}}{y_{n'} - y_{n'-1}} - \frac{x_{n'-1} - x_{n'-1-M'}}{y_{n'-1} - y_{n'-1-M'}} \right| \\ \text{s.t. } M' + 2 &\leq n' \leq N', 1 \leq x_{n'} \leq M_s, 1 \leq y_{n'} \leq N_s, \\ &y_{n'} - y_{n'-1} > 0, x_{n'} \in \mathbf{N}, y_{n'} \in \mathbf{N} \end{aligned} \tag{21}$$

where M' is a predesigned small number and $M' > 1$.

In this paper, the EMD method is utilized for the frequency estimation of the micro-Doppler frequency curves [30]. Applying the EMD method to the micro-Doppler curve of point scatterer at the cone top (or bottom), the frequencies $f_a + f_c$ and $|f_a - f_c|$ of the two sinusoidal components can be obtained. Thus, the estimated coning frequency \hat{f}_c is obtained.

After obtaining the coning frequency, the maximum value of micro-Doppler frequency curve can be obtained by taking the derivative with respect to Equation (20) in the slow-time domain.

$$\begin{aligned} f_{d'}(t_m) &= \frac{d(f_d(t_m))}{dt_m} \\ &= \frac{4\pi^2 a r}{\lambda R_0} \left(-(f_a - f_c)^2 (1 + \cos \theta_r) \sin(2\pi(f_a - f_c)t_m - \varphi_r) - (f_a + f_c)^2 (1 - \cos \theta_r) \sin(2\pi(f_a + f_c)t_m - \varphi_r) \right) \end{aligned} \tag{22}$$

where $f_{d'}(t_m)$ denotes the derivative of $f_d(t_m)$. Making $f_{d'}(t_m) = 0$, the slow-time t_{max} corresponding to the maximum value of $f_d(t_m)$ can be obtained.

$$(f_a - f_c)^2 (1 + \cos \theta_r) \sin(2\pi(f_a - f_c)t_{max} - \varphi_r) + (f_a + f_c)^2 (1 - \cos \theta_r) \sin(2\pi(f_a + f_c)t_{max} - \varphi_r) = 0 \tag{23}$$

The estimated values of rotation radius, \hat{r}_1 and \hat{r}_2 , can be obtained by the combination of \hat{f}_c and the maximum amplitudes of the two micro-Doppler frequency curves.

$$\hat{r}_i = \frac{\lambda \|f_{d-pci}(t_{max})\| R_i}{2\pi a \|A(t_{max})\|}, \quad i = 1, 2 \tag{24}$$

By the combination of (18) and (19), it can be obtained that

$$\begin{cases} R_0 - R_1 = (H - h) \cos \theta_c \\ r_1 = (H - h) \sin \theta_c \end{cases} \tag{25}$$

$$\begin{cases} R_2 - R_1 = H \cos \theta_c - r_c \sin \theta_c \\ r_2 + r_1 = H \sin \theta_c + r_c \cos \theta_c \end{cases} \quad (26)$$

From (25), the estimation of precession angle $\hat{\theta}_c$ can be obtained.

$$\hat{\theta}_c = \text{atan}\left(\frac{\hat{r}_1}{R_0 - \hat{R}_1}\right) \quad (27)$$

where, the observation values of R_1 and R_2 , which are \hat{R}_1 and \hat{R}_2 , can be obtained by setting a wideband radar at the origin point O . Substituting (27) into (26), the cone height can be estimated as

$$\hat{H} = (\hat{R}_2 - \hat{R}_1) \cos \hat{\theta}_c + (\hat{r}_1 + \hat{r}_2) \sin \hat{\theta}_c \quad (28)$$

The estimation of cone bottom radius \hat{r}_c can be obtained by substituting \hat{H} and $\hat{\theta}_c$ into (26).

$$\hat{r}_c = \frac{(\hat{r}_1 + \hat{r}_2) - \hat{H} \sin \hat{\theta}_c}{\cos \hat{\theta}_c} \quad (29)$$

Finally, the estimation of the distance from center O' to cone bottom (i.e., \hat{h}) can be written as

$$\hat{h} = \frac{\hat{r}_2 - \hat{r}_c \cos \hat{\theta}_c}{\sin \hat{\theta}_c} \quad (30)$$

So far, the coning frequency f_c , precession angle θ_c , cone height H , cone bottom radius r_c , and the distance from center O' to cone bottom (i.e., h) are all estimated.

For better understanding, the flow chart of the proposed method is presented as Figure 4.

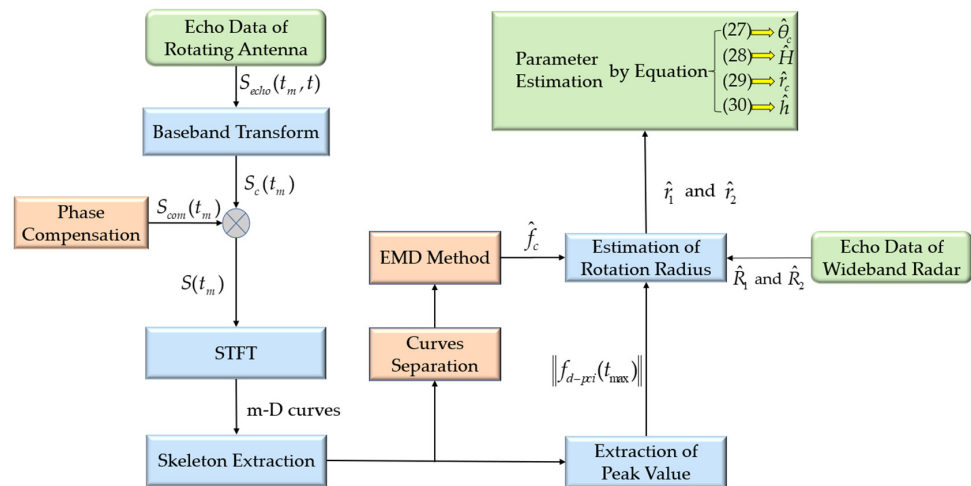


Figure 4. Flowchart of the proposed method.

4. Simulation Results and Discussions

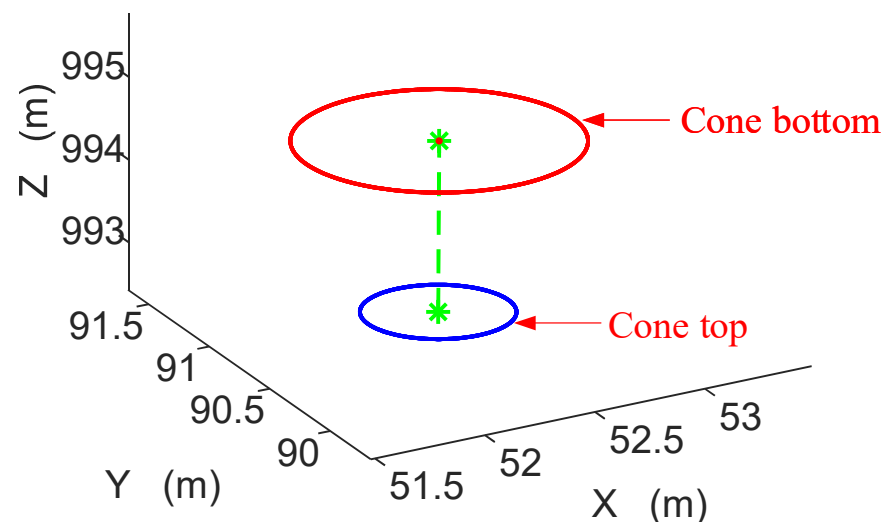
4.1. Validation of the Algorithm

The simulation parameters of radar and target are shown in Table 1.

Table 1. Simulation parameters of radar and target.

Category	Parameter	Value	Unit
Radar	Carrier frequency of rotating antenna	75	GHz
	Transmitted bandwidth of wideband radar	2	GHz
	PRF of rotating antenna	400	Hz
	Carrier frequency of wideband radar	10	GHz
	PRF of wideband radar	1000	Hz
	Antenna's rotation radius	10	m
	Antenna's rotation frequency	2	Hz
	Observation time	1	s
	Signal to noise ratio (SNR)	15	dB
Target	Coordinates of the centroid	$(1000, \pi/30, \pi/3)$	(m, rad, rad)
	Cone height	2	m
	Radius of cone bottom	0.5	m
	Precession angle	$\pi/15$	rad
	Coning frequency	6	Hz
	Distance from centroid to cone bottom	0.5	m

The trajectories of scatterers at the cone top and bottom are shown in Figure 5. The rotation centers of the cone top and bottom are located at $(52.19, 90.39, 993.06)$ m and $(52.28, 90.56, 994.90)$ m respectively. Therefore, the rotation centers of the two scatterers are both in the radar LOS.

**Figure 5.** The trajectories of the scatterer points at the cone top and bottom.

First, the high-resolution 1D range sequences of two scatterers are obtained by the wideband radar. Because the micro-motion component is perpendicular to the radar LOS, the 1D range sequences of the target are two straight lines on the slow-time-range plane. The imaging results are shown in Figure 6. The normalized amplitude reaches the peak when the ranges are 998.5 m and 1000.35 m. Therefore, the estimated ranges of the two scatterers at cone top and bottom are 998.5 m and 1000.35 m respectively.

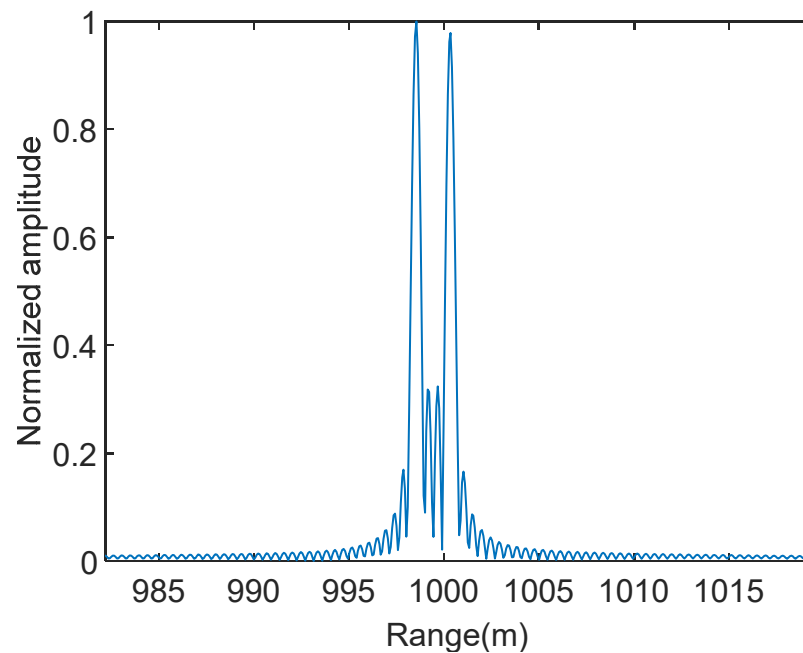


Figure 6. High-resolution 1D ranges of the two scatterers at cone top and bottom.

The STFT is performed on $S(t_m)$ to obtain the slow-time-varying micro-Doppler frequency curves of the two scatterers, as shown in Figure 7a. The theoretical rotation radius of cone top and bottom are 0.3119 m and 0.593 m respectively, and the coning frequencies are both 6 Hz. The amplitude of the echo micro-Doppler frequency corresponding to the cone bottom scatterer is 72 Hz, which is greater than that corresponding to the cone top scatterer (i.e., 40 Hz). Through Equation (20), the theoretical micro-Doppler frequency curves can be drawn, as shown in Figure 7b. The amplitudes of theoretical micro-Doppler frequency curves are 74.66 Hz and 38.87 Hz respectively. It can be found that the echo micro-Doppler frequency curves are completely coincident with the theoretical one.

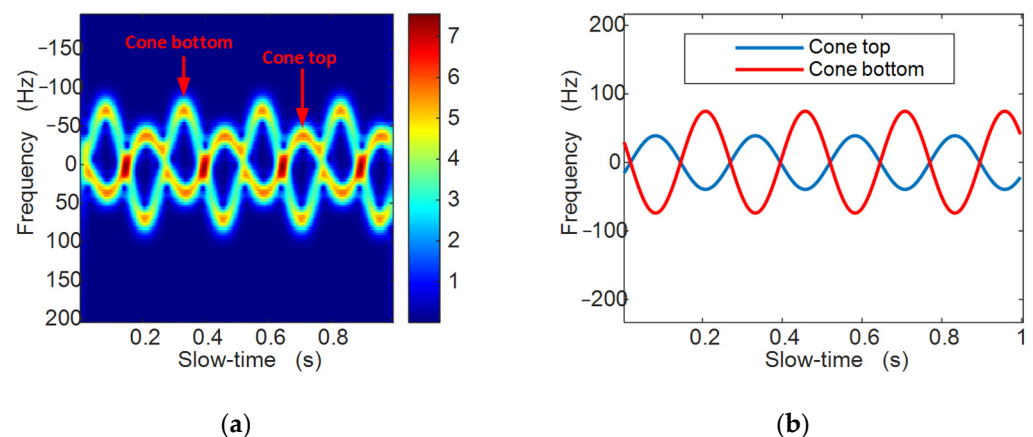


Figure 7. Simulations of the micro-Doppler effect of the precession cone-shaped target perpendicular to the radar LOS. (a) Echo micro-Doppler frequency curves. (b) Theoretical micro-Doppler frequency curves.

To improve the precision of time-frequency analysis, the skeleton extraction algorithm is utilized to extract the skeleton of the micro-Doppler frequency curve. First, in order to eliminate the interference of noise points nearby in Figure 7a, a Gaussian spatial mask with pixels 3×3 is used to smooth the micro-Doppler frequency curve, as shown in Figure 8a. Second, Figure 8a is further converted into a binary image, where black represents 0 and

white represents 1, as shown in Figure 8b. Finally, skeleton extraction is carried out for Figure 8b, as shown in Figure 8c.

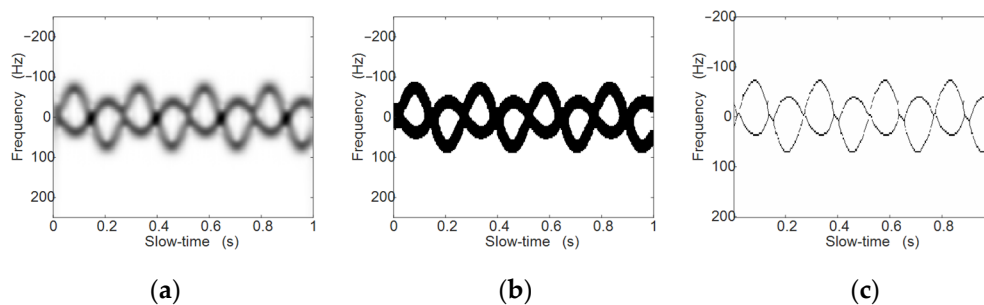


Figure 8. Skeleton extraction of echo micro-Doppler frequency curve. (a) Result of smooth processing. (b) Result of binarization processing. (c) Result of skeleton extraction.

The skeletons of the micro-Doppler curves are separated, and the separation results are shown in Figure 9.

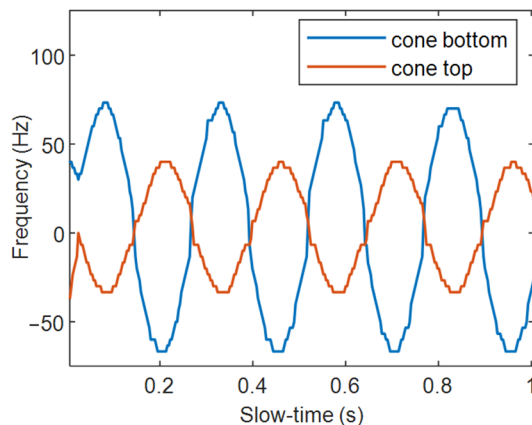


Figure 9. The separation results of micro-Doppler curves.

After the separation of micro-Doppler curves, the EMD method is applied to decompose the micro-Doppler curve of point scatterer at the cone top (or bottom). The decomposition results are shown in Figure 10a, and the energy ratio of each decomposition signal is shown in Figure 10b. Since the Gaussian mask and binarization operation significantly suppress the interference of noise on EMD decomposition, the energy proportion of the high-frequency component generated by noise is very small compared with that of the micro-Doppler signal components. In addition, the quantization error determined by the length of the slow-time sampling unit will lead to the step shape of the separated curves, thus introducing the high frequency component, but its energy proportion is also very small. Based on the above facts, the micro Doppler signal components can be easily distinguished in the figure of energy proportion. According to Equation (20), when $\theta_r = \pi/30$ rad, the ratio of the amplitude of the signal component with frequency $(f_c - f_a)$ to that of the signal component with frequency $(f_c + f_a)$ is $\frac{(f_c - f_a)(1 + \cos \theta_r)}{(f_c + f_a)(1 - \cos \theta_r)} = 182$, and the ratio of energy is 33,124. Therefore, the frequency of IMF2 with the highest energy proportion is $(f_c - f_a)$. The period of IMF2 is $\frac{1}{f_c - f_a} = 0.25$ s, so the coning frequency can be estimated as $\hat{f}_c = 6$ Hz. IMF1 is the high frequency component, IMF2 is the micro-Doppler signal component with frequency $(f_c - f_a)$, whose energy proportion is the highest. The remaining components are the residual low frequency components.

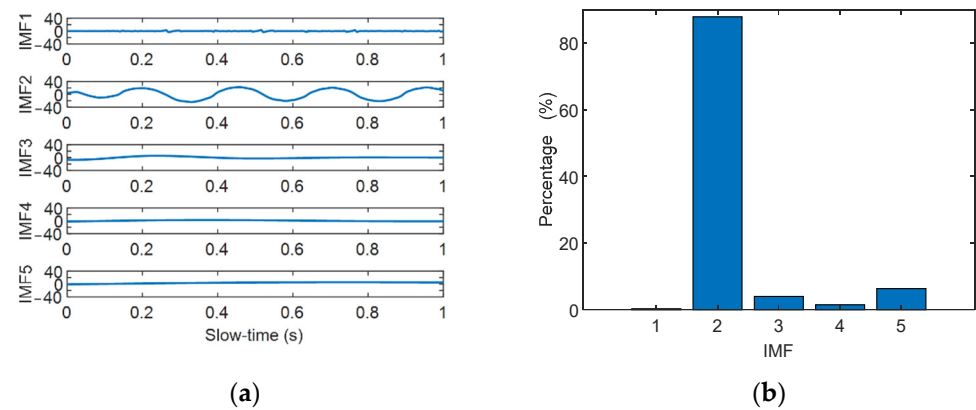


Figure 10. Estimation results of the coning frequency by using the EMD method. (a) Decomposition results of micro-Doppler frequency shift. (b) The energy ratio of each decomposition signal.

Next, the estimated coning frequency is used to derive the maximum value of micro-Doppler frequency curve. The change process of $f_d'(t_m)$ with slow-time is shown in Figure 11. Make $f_d'(t_m) = 0$, the slow-time (within a period) corresponding to the maximum value are $t_{max} = 0.3333$ s or 0.457 s, and $A(t_{max}) = 7.9756$. According to Equation (23), $\hat{r}_1 = 0.3178$ m and $\hat{r}_2 = 0.5731$ m.

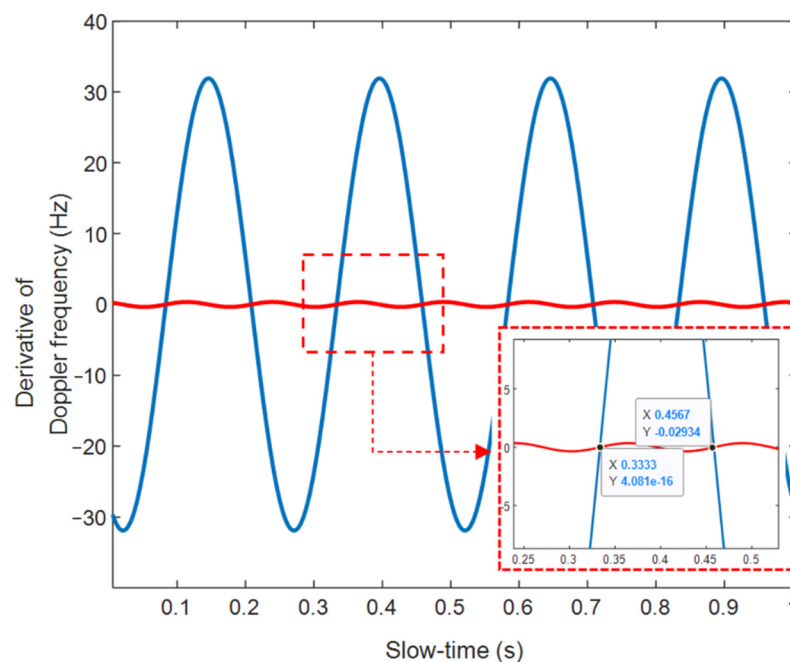


Figure 11. Derivative of micro-Doppler frequency curve with slow-time.

In order to evaluate the estimation performance of the proposed algorithm, the mean absolute percentage error (MAPE) is introduced.

$$MAPE = \frac{100\%}{\dot{N}} \sum_{n=1}^{\dot{N}} \left| \frac{y(n) - y}{y} \right| \quad (31)$$

where \dot{N} is the number of Monte Carlo experiments, $y(n)$ represents the estimated value of parameter y in the n – th experiment. In this paper, \dot{N} is set as 100, which means that Monte Carlo experiments are carried out 100 times under different conditions.

The MAPEs of the proposed method are shown in Table 2. The MAPEs of the geometric parameters are all below 8%, among which the MAPEs of the cone height and the cone bottom radius are only 0.28% and 2.38% respectively. The MAPEs of micro-motion parameters are all below 0.5%, among which the MAPEs of coning frequency and precession angle are only 0% and 0.31% respectively. The simulations above verify the effectiveness of the proposed method.

Table 2. MAPEs of precession cone-shaped target parameters (SNR = 15 dB).

Parameter	True Value	Estimated Value	MAPE
f_c	6.0 Hz	6.0 Hz	0%
r_c	0.5 m	0.4881 m	2.38%
H	2.0 m	1.9945 m	0.28%
θ_c	$\pi/15$ rad	0.2088 rad	0.31%
h	0.5 m	0.4612 m	7.76%

4.2. Performance Analysis of Proposed Algorithm

The effect of range on the MAPE is analyzed below. The approximation error of radial distance can be expressed as the absolute value of the difference between (8) and (9). Monte Carlo experiments are carried out 100 times under the different radial distances conditions to investigate the effect of range on approximation error of radial distance. The change process of approximate error with range is shown in Figure 12. The approximation error decreases as range increases. When $R_0 = 1000$ m, the approximate error of the radial distance is only 2 mm, which is so small compared to the operating wavelength ($\lambda = 4$ mm) that the effect on the phase is negligible.

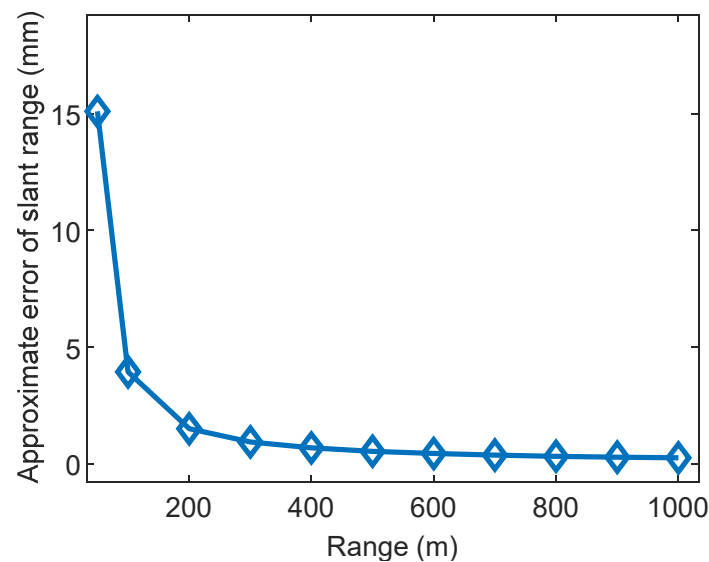


Figure 12. Approximate range errors of different radial distances.

The 11 radial distances above are chosen to investigate the effect of range on the MAPE of f_c , H , θ_c , r_c , and h . The average MAPEs of five parameters under the conditions different radial distances are shown in Figure 13. As the radial distance increases, the approximate error is reduced and the estimation performance of the proposed method is improved.

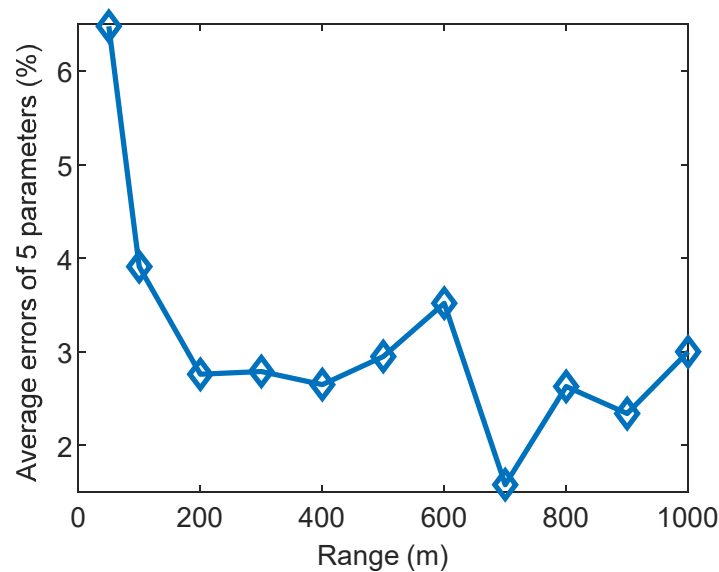


Figure 13. The change process of average errors of five parameters with different ranges.

Next, the influence of the coning frequency on parameters estimation accuracy is studied. It can be seen from Equation (20), when the coning frequency of target increases, the micro-Doppler spectral width will increase. In order to guarantee the Nyquist sampling to micro-Doppler spectrum, the PRF of rotating antenna should be greater than two times of the micro-Doppler spectrum width, otherwise the micro-Doppler signal will overlap in the frequency domain, which puts forward higher requirements for the PRF of the rotating antenna. When the coning frequencies are 6 Hz, 20 Hz, 40 Hz, and 60 Hz respectively, and the corresponding PRFs are set as 400 Hz, 1000 Hz, 2400 Hz, and 3200 Hz respectively. The estimated values of the coning frequencies obtained by EMD method are 6 Hz, 20.0833 Hz, 40.0228 Hz, and 59.8035 Hz, respectively. When the derivative of micro Doppler frequency is 0, the slow-times t_{max} are selected as 0.457 s, 0.4055 s, 0.377 s and 0.3 s respectively, and the corresponding values of $A(t_{max})$ are 7.9756, 36.096, 75.7316, and 114.9811 respectively. The micro-Doppler frequency extreme values of the point scatterers at the cone bottom and top at the slow-times t_{max} are (72 Hz, 40 Hz), (330.3 Hz, 180.5 Hz), (694.2 Hz, 370.7 Hz), and (1058 Hz, 553.3 Hz) respectively. Thus, the rotation radius of the point scatterers at the cone bottom and top can be calculated as (0.5731 m, 0.3178 m), (0.5827 m, 0.3179 m), (0.5838 m, 0.3112 m), and (0.5863 m, 0.3061 m) respectively. Based on this, estimated values of precession angle, cone height, cone bottom radius, and distance from center to cone bottom can be estimated in Table 3. The variation of MAPEs with coning frequency is shown in Figure 14. It can be seen that the parameters information of the cone-shaped target can be obtained accurately and effectively by the proposed method under the conditions of high speed rotation of the target.

Table 3. The estimated values of the five parameters under different coning frequencies.

f_c	\hat{f}_c	$\hat{\theta}_c$	\hat{H}	\hat{r}_c	\hat{h}
6 Hz	6 Hz	0.2088 rad	1.9945 m	0.4881 m	0.4612 m
20 Hz	20.0833 Hz	0.2088 rad	1.9965 m	0.4975 m	0.4632 m
40 Hz	40.0228 Hz	0.2045 rad	1.9932 m	0.5005 m	0.4613 m
60 Hz	59.8035 Hz	0.2013 rad	1.9911 m	0.5045 m	0.4602 m

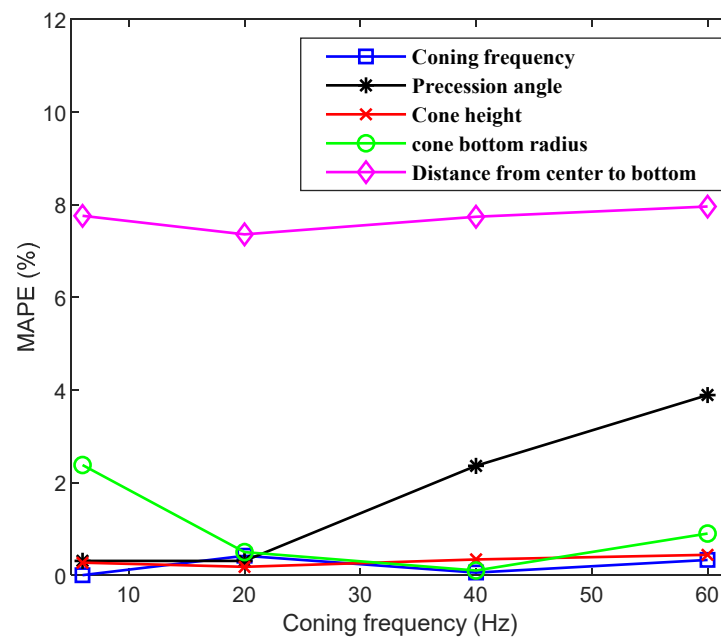


Figure 14. MAPEs of five parameters with different coning frequencies.

In Figure 4, it can be seen that the estimation of rotation radius is the key procedure of the proposed method. Equations (27)–(30) are all related to the rotation radius. According to Equation (23), the coning frequency obtained by EMD method will affect the estimated value of the micro-Doppler extreme point, thus determining the estimation accuracy of the rotation radius. Next, the influence of the normalized coning frequency error on the estimation accuracy of the other four parameters will be explored. The true value of coning frequency is 6 Hz. When its normalized error varies between -10% and 10% , the other four parameters estimation results are shown in Table 4, and the MAPEs of the other four parameters are shown in Figure 15. In general, the estimation errors of the other four parameters increase with the increase of the normalized error of the coning frequency.

Table 4. The estimated values of the other four parameters with different normalized error of coning frequency.

Normalized Error of f_c	$\hat{\theta}_c$	\hat{H}	\hat{r}_c	\hat{h}
-10%	0.2453 rad	2.0558 m	0.5940 m	0.5095 m
-5%	0.2259 rad	2.0241 m	0.5478 m	0.4850 m
0%	0.2094 rad	1.9993 m	0.5083 m	0.4658 m
5%	0.1952 rad	1.9796 m	0.4744 m	0.4506 m
10%	0.1829 rad	1.9637 m	0.4449 m	0.4382 m

The anti-noise ability of the proposed method is tested by adding complex Gaussian white noise into the echo signal. When SNR is -10 dB, the echo micro-Doppler curves and skeletons are shown in Figure 16a,b. The echomicro-Doppler curves are heavily contaminated by the noise, and the Gaussian spatial mask and binarization operation can no longer effectively suppress noise. The skeletons are not smooth, so the micro-Doppler curves cannot be effectively separated.

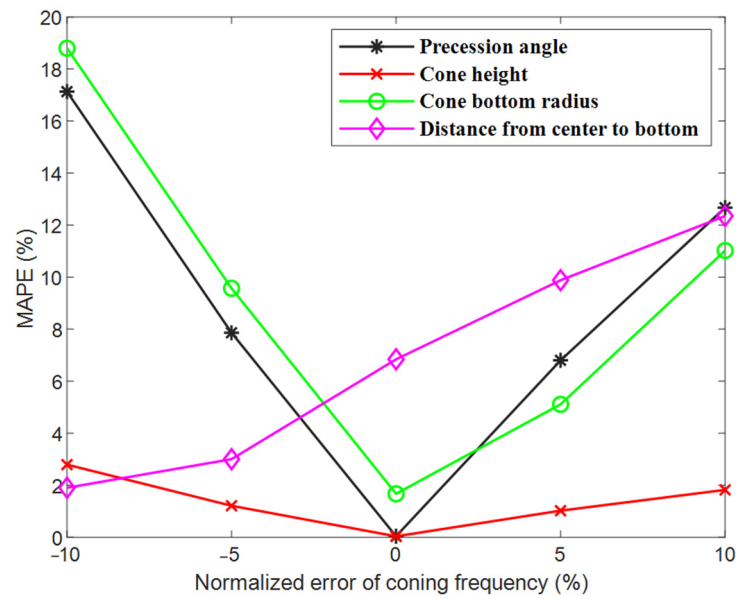


Figure 15. MAPEs of the other four parameters with different normalized error of coning frequency.

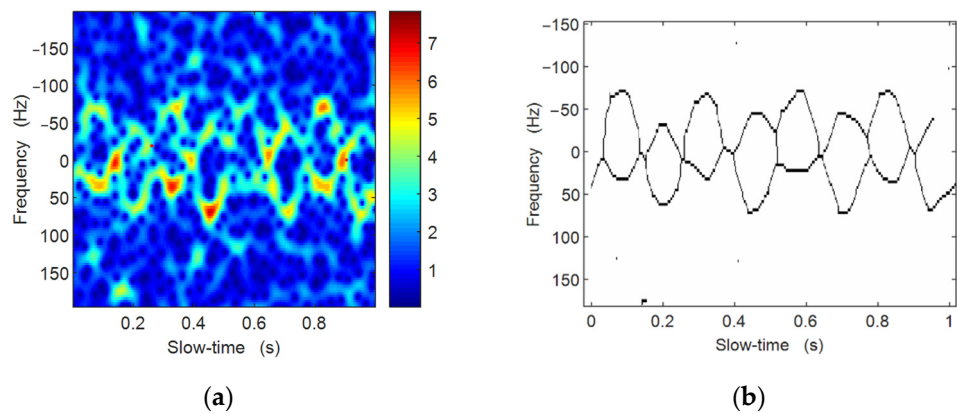


Figure 16. The echo micro-Doppler curves and skeletons when SNR is -10 dB. (a) Echo micro-Doppler curves. (b) Skeletons of echo micro-Doppler curves.

When the SNR is -5 dB, the echo micro-Doppler curves, skeletons, and curve separation results are shown in Figure 17a–c respectively. It can be concluded that when the SNR is higher than -5 dB, the parameters of the precession cone-shaped target can be estimated effectively by the proposed method, and the estimation effect will be discussed below.

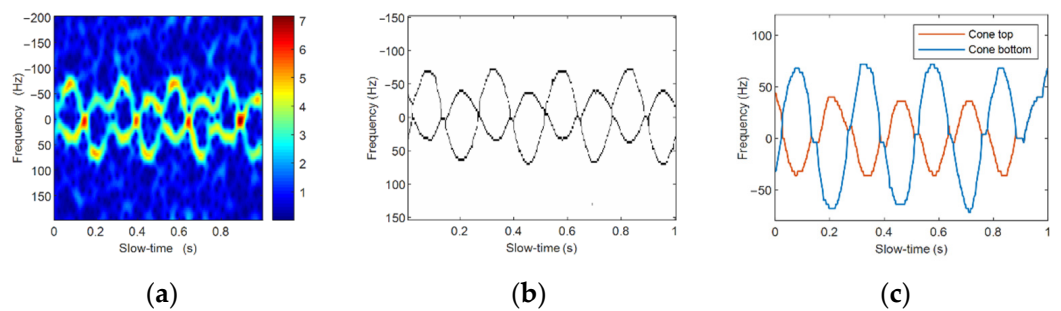


Figure 17. The echo micro-Doppler curves, skeletons and curve separation results when SNR is -5 dB. (a) Echo micro-Doppler curves. (b) Skeletons of echo micro-Doppler curves. (c) Curve separation results.

The simulation experiments are carried out in six groups of different noise environments. Monte Carlo simulations are carried out 100 times under the conditions of different SNRs. SNRs are set as -5 dB, 0 dB, 5 dB, 10 dB, 15 dB, 20 dB respectively. The change process of MAPE with SNR is shown in Figure 18. The parameters estimation accuracy increases with the improvement of SNR. The reason is that the improvement of SNR improves the extraction accuracy of the 1D range and micro-Doppler frequency. Compared with the other four parameters, the estimation accuracy of h is lower for the following reason: h is the last parameter to be estimated, and the estimation of h depends on the estimation of other parameters, so the error caused by SNR will accumulate to the maximum on h . The estimation accuracy of coning frequency is the highest among the five parameters, mainly because the period is directly estimated by the EMD method.

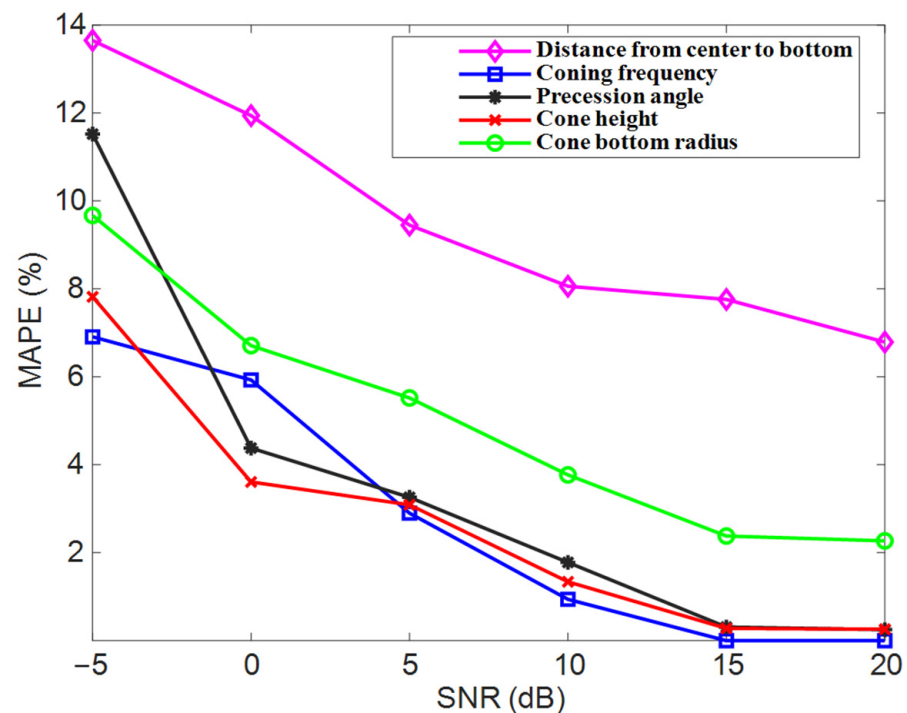


Figure 18. MAPE under different SNRs.

The parameters estimation performance of the proposed method is closely related to the extraction accuracies of 1D range and micro-Doppler frequency, and the extraction accuracies of 1D range and micro-Doppler frequency are related to the range resolution of wideband radar and the resolution of time-frequency analysis respectively. In order to test the effect of the 1D range extraction accuracy on the parameter's estimation performance, range resolutions of wideband radar are set as 0.4 m, 0.3 m, 0.2 m, 0.1 m, 0.05 m, and 0.025 m respectively. The change process of MAPE with range resolution is shown in Figure 19. In general, the higher the range resolution is, the smaller the MAPE is.

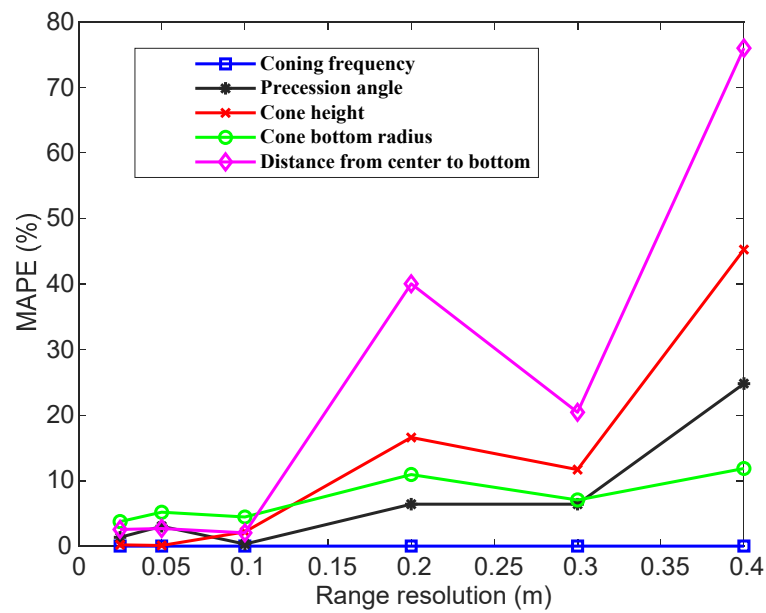


Figure 19. MAPE of five parameters with different range resolutions.

The estimation error of Doppler frequency shift ΔF is defined as

$$\Delta F = F - \hat{F} \tag{32}$$

where F represents the true value and \hat{F} represents the estimated value. ΔF follows a uniform distribution with $\Delta F \sim U(-10\text{Hz}, 10\text{Hz})$. The change process of MAPE with ΔF is shown in Figure 20. The MAPE increases linearly as the absolute value of ΔF increases.

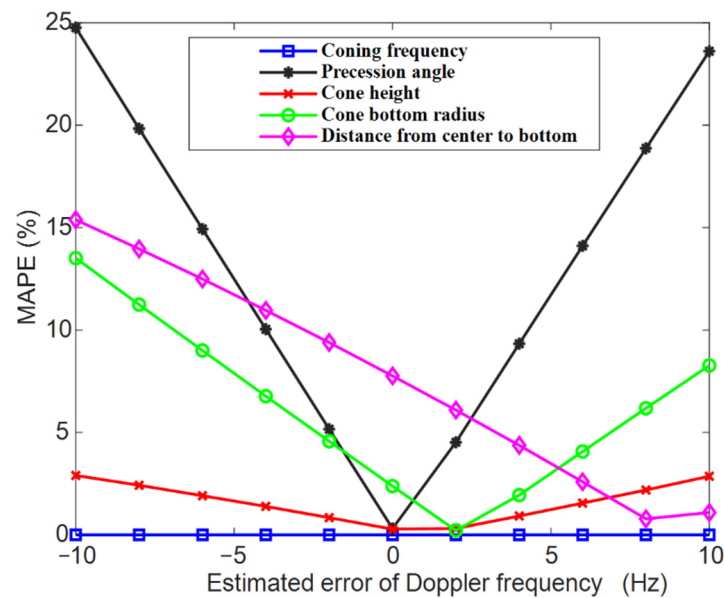


Figure 20. MAPE of five parameters with different estimation errors of micro-Doppler frequency.

It can be found from the above analysis that the key to obtain high-accuracy parameters is to improve the range resolution of wideband radar and the resolution of the time-frequency analysis.

4.3. Comparison with Other Method

In order to verify the superiority of the proposed method, it is compared with the method proposed in [24]. The parameters of target are set as $H = 2$ m, $r_c = 0.5$ m, $\theta_c = \pi/15$ rad, $f_c = 4$ Hz, $h = 0.5$ m and $R_0 = 20$ m.

In [24], the radius a of UCA and OAM mode number α are set as 0.5 m and 30 respectively. The echo angular Doppler and theoretical angular Doppler curves are shown in Figure 21a,b respectively. However, large OAM mode number requires a large number of array elements. If $\alpha = 30$, a minimum of 62 antennas are required, which is high in cost.

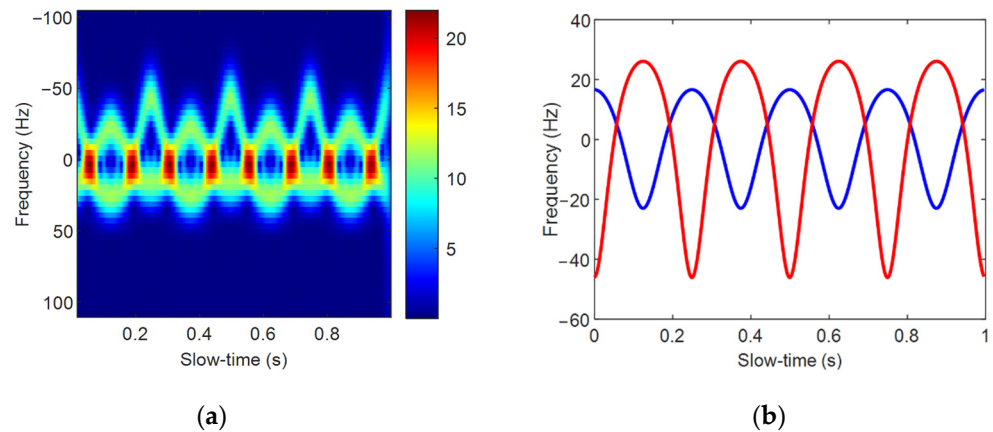


Figure 21. The angular Doppler effect in [24]. (a) Echo angular Doppler curve. (b) Theoretical angular Doppler curve.

The results shown in Table 5 indicate that the MAPE of the parameter estimation method proposed in this paper is significantly lower than the method proposed in [24], which illustrates the effectiveness of the proposed method.

Table 5. Comparison of MAPEs between the proposed method and the method in [24]. (SNR = 15 dB).

Method	f_c	θ_c	H	r_c	h
Method in [24]	1.47%	2.83%	0.52%	8.52%	18.22%
Proposed method	0%	0.07%	0.14%	1.68%	2.18%

5. Conclusions

In order to estimate the precession cone-shaped target parameters under the condition that the micro-motion plane is perpendicular to the radar LOS. First, a new radar configuration is designed, whose antenna rotates at a steady speed in a fixed circle, thus producing Doppler frequency shift. Second, the expression of the micro-Doppler frequency induced by the precession cone-shaped target is derived. Then, the curve separation is realized by using the smoothness of micro-Doppler curves, and the EMD method is utilized for the detection and estimation of the coning frequency. Finally, the micro-motion components perpendicular to the radar LOS are inverted by the peak of micro-Doppler frequency curve. Compared with distributed radar network, the proposed method overcomes the difficulty of data co-processing. Compared with vortex EM radar, the proposed method can realize the parameters estimation of cone-shaped targets with only a rotating antenna, so the application cost of the proposed method is lower. Moreover, the parameters estimation accuracies are improved obviously. When the SNR is higher than -5 dB, the proposed method can extract the parameters of the precession cone-shaped targets effectively. The simulation results show the advantages of this novel method. The proposed method provides a new idea for the high-precision extraction of precession cone-shaped targets in the special scene.

In this paper, 75 GHz millimeter-wave is taken as an example to verify the effectiveness and robustness of the proposed method in theoretical and simulation experiments. The feasibility of the proposed method will be verified in practical scenarios in the next step, which requires consideration of the atmospheric transmission band (around 35 GHz or around 94 GHz) of millimeter-wave radars.

The method proposed in this paper can effectively extract the micro-motion parameters perpendicular to the radar LOS by taking advantage of the angular diversity of observation brought by the rotating antenna. The superiority of the proposed method is demonstrated by this special scenario. When the target trajectory does not match the radar LOS, the 3D micro-motion features of the target are expected to be extracted by using the angular diversity of observation brought by the rotating antenna, which will be our next research direction.

Author Contributions: Conceptualization and methodology, Z.W.; software, Z.W.; resources, Y.L.; writing—review and editing, Z.W., Y.L., K.L., H.Y., and Q.Z. All authors have read and agreed to the published version of the manuscript.

Funding: This research was funded by the National Nature Science Foundation of China under Grant 61971434 and 62131020.

Data Availability Statement: Not applicable.

Conflicts of Interest: The authors declare no conflict of interest.

References

1. Chen, V.C.; Li, F.; Ho, S.S.; Wechsler, H. Micro-Doppler effect in radar: Phenomenon, model, and simulation study. *IEEE Trans. Aerosp. Electron. Syst.* **2006**, *42*, 2–21. [\[CrossRef\]](#)
2. Chen, X.; Guan, J.; Liu, N.; Zhou, W.; He, Y. Detection of a Low Observable Sea-Surface Target with Micromotion via the Radon-Linear Canonical Transform. *IEEE Geosci. Remote Sens. Lett.* **2014**, *11*, 1225–1229. [\[CrossRef\]](#)
3. Du, L.; Li, L.; Wang, B.; Xiao, J. Micro-Doppler Feature Extraction Based on Time-Frequency Spectrogram for Ground Moving Targets Classification with Low-Resolution Radar. *IEEE Sens. J.* **2016**, *16*, 3756–3763. [\[CrossRef\]](#)
4. Chen, X.; Guan, J.; Li, X.; He, Y. Effective coherent integration method for marine target with micromotion via phase differentiation and radon-Lv's distribution. *IET Radar Sonar Navig.* **2015**, *9*, 1284–1295. [\[CrossRef\]](#)
5. Abdullah, R.S.A.R.; Alnaeb, A.; Salah, A.A.; Rashid, N.E.A.; Sali, A.; Pasya, I. Micro-Doppler Estimation and Analysis of Slow Moving Objects in Forward Scattering Radar System. *Remote Sens.* **2017**, *9*, 699. [\[CrossRef\]](#)
6. Chen, X.; Guan, J.; Huang, Y.; Liu, N.; He, Y. Radon-linear canonical ambiguity function-based detection and estimation method for marine target with micro motion. *IEEE Trans. Geosci. Remote Sens.* **2015**, *53*, 2225–2240. [\[CrossRef\]](#)
7. Amiri, R.; Shahzadi, A. Micro-Doppler based target classification in ground surveillance radar systems. *Digit. Signal Process.* **2020**, *101*, 102702. [\[CrossRef\]](#)
8. Ren, K.; Du, L.; Lu, X.; Zhuo, Z.; Li, L. Instantaneous Frequency Estimation Based on Modified Kalman Filter for Cone-Shaped Target. *Remote Sens.* **2020**, *12*, 2766. [\[CrossRef\]](#)
9. Zhuo, Z.; Zhou, Y.; Du, L.; Ren, K.; Li, Y. A Noise Robust Micro-Range Estimation Method for Precession Cone-Shaped Targets. *Remote Sens.* **2021**, *13*, 1820. [\[CrossRef\]](#)
10. Zhang, W.; Fu, Y.W.; Nie, L.; Zhao, G.H.; Yang, W.; Yang, J. Parameter estimation of micro-motion targets for high-range-resolution radar using high-order difference sequence. *IET Signal Process.* **2018**, *12*, 1–11. [\[CrossRef\]](#)
11. Zhou, Y.; Chen, Z.Y.; Zhang, L.R.; Xiao, J.G. Micro-doppler curves extraction and parameter estimation for cone-shaped target with occlusion effect. *IEEE Sens. J.* **2018**, *18*, 2892–2902. [\[CrossRef\]](#)
12. Han, L.; Feng, C. Parameter Estimation for Precession Cone-Shaped Targets Based on Range-Frequency-Time Radar Data Cube. *Remote Sens.* **2022**, *14*, 1548. [\[CrossRef\]](#)
13. Bai, X.R.; Bao, Z. High-Resolution 3D Imaging of Precession Cone-Shaped Targets. *IEEE Trans. Antennas Propag.* **2014**, *62*, 4209–4219. [\[CrossRef\]](#)
14. He, X.Y.; Tong, N.N.; Hu, X.W. High-resolution Imaging and Three-dimensional Reconstruction of Precession Targets by Exploiting Sparse Apertures. *IEEE Trans. Aerosp. Electron. Syst.* **2017**, *53*, 1212–1220. [\[CrossRef\]](#)
15. Luo, Y.; Zhang, Q.; Yuan, N.; Zhu, F.; Gu, F.F. Three-dimensional precession feature extraction of space targets. *IEEE Trans. Aerosp. Electron. Syst.* **2014**, *50*, 1313–1329. [\[CrossRef\]](#)
16. Luo, Y.; Chen, Y.-A.; Sun, Y.; Zhang, Q. Narrowband Radar Imaging and Scaling for Space Targets. *IEEE Geosci. Remote Sens. Lett.* **2017**, *14*, 1–5. [\[CrossRef\]](#)
17. Choi, I.O.; Park, S.H.; Kang, K.B.; Lee, S.H.; Kim, K.T. Efficient parameter estimation for cone-shaped target based on distributed radar networks. *IEEE Sens. J.* **2019**, *19*, 9736–9747. [\[CrossRef\]](#)

18. Choi, I.O.; Park, S.H.; Kim, M.; Kang, K.B.; Kim, K.T. Efficient Discrimination of Ballistic Targets with Micromotions. *IEEE Trans. Aerosp. Electron. Syst.* **2020**, *56*, 1243–1261. [[CrossRef](#)]
19. Persico, A.R.; Clemente, C.; Gaglione, D.; Ilioudis, C.V.; Cao, J.; Pallotta, L.; De Maio, A.; Proudler, I.K.; Soraghan, J.J. On Model, Algorithms, and Experiment for Micro-Doppler-Based Recognition of Ballistic Targets. *IEEE Trans. Aerosp. Electron. Syst.* **2017**, *53*, 1088–1108. [[CrossRef](#)]
20. Liu, K.; Cheng, Y.Q.; Li, X.; Jiang, Y.W. Passive OAM-Based Radar Imaging with Single-In-Multiple-Out Mode. *IEEE Microw. Wirel. Compon. Lett.* **2018**, *28*, 840–842. [[CrossRef](#)]
21. Zhou, Z.L.; Cheng, Y.Q.; Liu, K.; Wang, H.Q.; Qin, Y.L. Rotational Doppler Resolution of Spinning Target Detection Based on OAM Beams. *IEEE Sens. J.* **2019**, *3*, 1–4. [[CrossRef](#)]
22. Wang, J.Q.; Liu, K.; Cheng, Y.Q.; Wang, H.Q. Three-Dimensional Target Imaging Based on Vortex Stripmap SAR. *IEEE Sens. J.* **2019**, *19*, 1338–1345. [[CrossRef](#)]
23. Wang, Y.; Liu, K.; Wang, J.Q.; Wang, H.Q. Rotational Doppler detection of a cone-shaped target under the illumination of a vortex electromagnetic wave. *Radars. J.* **2021**, *10*, 740–748.
24. Gong, T.; Cheng, Y.Q.; Li, X.; Chen, D.C. Micromotion Detection of Moving and Spinning Object Based on Rotational Doppler Shift. *IEEE Microw. Wirel. Compon. Lett.* **2018**, *28*, 843–845. [[CrossRef](#)]
25. Wang, Y.; Liu, K.; Liu, H.Y.; Wang, J.Q.; Cheng, Y.Q. Detection of Rotational Object in Arbitrary Position Using Vortex Electromagnetic Waves. *IEEE Sens. J.* **2021**, *21*, 4989–4994. [[CrossRef](#)]
26. Luo, Y.; Chen, Y.J.; Zhu, Y.Z.; Li, W.Y.; Zhang, Q. Doppler effect and micro-Doppler effect of vortex-electromagnetic-wave-based radar. *IET Radar Sonar Navig.* **2019**, *14*, 2–9. [[CrossRef](#)]
27. Chen, R.; Zhou, H.; Moretti, M.; Wang, X.; Li, J. Orbital Angular Momentum Waves: Generation, Detection, and Emerging Applications. *IEEE Commun. Surv. Tutor.* **2020**, *22*, 840–868. [[CrossRef](#)]
28. Liu, K.; Liu, H.Y.; Qin, Y.L.; Cheng, Y.Q.; Wang, S.N.; Li, X.; Wang, H.Q. Generation of OAM Beams Using Phased Array in the Microwave Band. *IEEE Trans. Antennas Propag.* **2016**, *64*, 3850–3857. [[CrossRef](#)]
29. Chen, X.; Guan, J.; Bao, Z.; He, Y. Detection and extraction of target with micro motion in spiky sea clutter via short-time fractional Fourier transform. *IEEE Trans. Geosci. Remote Sens.* **2014**, *52*, 1002–1018. [[CrossRef](#)]
30. Zhu, N.; Hu, J.; Xu, S.; Wu, W.; Zhang, Y.; Chen, Z. Micro-Motion Parameter Extraction for Ballistic Missile with Wideband Radar Using Improved Ensemble EMD Method. *Remote Sens.* **2021**, *13*, 3545. [[CrossRef](#)]